

Fractional crystallisation of eclogite during the birth of a Hawaiian Volcano

Laura A. Miller ^{1,2}✉, Hugh St. C. O'Neill ¹, Andrew J. Berry ² & Charles Le Losq³

The initial melts erupted by a Hawaiian volcano have a range of alkalic compositions but are rarely observed as they are covered by enormous volumes of shield stage tholeiites. A remarkable record of the early evolution of Hawaiian volcanoes, however, is preserved by a volcanic sandstone dredged from the submarine flank of Kilauea, which contains a suite of petrogenetically related pre-shield basanite to nephelinite glasses. Here we show that the systematic variation in the rare earth element (REE) patterns of these samples requires the fractional crystallisation of garnet. A fractionating assemblage of Ca-rich garnet (32%), omphacitic clinopyroxene (63%), and minor phlogopite can explain the variation in the major and trace element contents of the suite. The results suggest fractional crystallisation of eclogite from a primitive Hawaiian melt near the base of the lithosphere (>90 km) and that a deep magma chamber is the first stage in the development of a Hawaiian volcano.

¹School of Earth, Atmosphere and Environment, Monash University, Clayton, VIC 3800, Australia. ²Research School of Earth Sciences, Australian National University, Canberra, ACT 2601, Australia. ³Université Paris Cité, Institut de Physique du Globe de Paris, CNRS, F-75005 Paris, France.
✉email: laura.miller@monash.edu

The birth of a Hawaiian volcano is an enigmatic stage in its growth. The lifecycle of an oceanic intraplate volcano is thought to evolve from an alkalic pre-shield stage with a moderately deep magma chamber (<30 km), to a tholeiitic shield-stage with a shallow magma chamber (<3 km) that produces 95% of the erupted products, before a return to alkalic magmatism in a post-shield stage^{1–4}. The degree of melting varies throughout these stages with low degrees of melting at the edge of the plume generating the low SiO₂, alkalic melts⁵. The youngest Hawaiian volcano, Loihi, is already entering shield-stage volcanism, while the pre-shield products of older Hawaiian volcanoes have been covered by vast amounts of tholeiitic shield-stage basalt. As a result, very little is known about the inception of Hawaiian volcanism with the scarcity of samples limiting our understanding of the low-degree melts generated during this early stage.

Volcaniclastic sandstones dredged from the south-eastern flank of Kilauea (site S508; Fig. 1 in Coombs et al.⁶) contain hyaloclastic spherules (Fig. S1) with a wide range of melt compositions, many of which are attributed to the pre-shield stage of Kilauea^{3,7}. Among these glasses, are a set of 22 samples that exhibit a smooth continuous change in composition from basanite (sample B11) to nephelinite (sample C4), and progressive enrichment and depletion of incompatible and compatible elements, respectively (Tables S1 and S2; see group 1 glasses in Fig. 1 and Fig. 2 of Sisson et al.⁸). The glasses have trace element ratios that are distinct from prominent geochemical reservoirs (Table S3). For example, the average Ba/Th (ppm) is 350 ± 30 , which exceeds that of both the bulk silicate Earth and ocean floor basalts (~80^{9,10}), and typical Hawaiian tholeiites (80–200¹¹). Further, many ratios of the most incompatible trace elements are essentially identical in the least and most evolved members of the suite (Table S3). The smooth change in major and trace element compositions and constant trace element ratios indicate that a single process formed the suite of glasses, for example, fractional crystallisation of an evolving melt, partial melting of a common source, or mixing of two melts that originated from the same source. That these glasses are a rare example of pre-shield magmatism and are petrogenetically linked endows them with considerable value.

Here, we address the petrogenesis of the suite of pre-shield basanite–nephelinite glasses from Kilauea by modelling the evolution of the REE patterns and the variations in trace element and major element compositions, for partial melting, fractional crystallisation, reactive melt flow and binary mixing. The changes in the REE patterns can only be reproduced by the fractional crystallisation of garnet, while the changes in trace and major element concentrations are consistent with the fractionation of eclogite. This implies the presence of a deep magma chamber during the inception of a Hawaiian volcano.

Results and discussion

The petrogenesis of Hawaiian pre-shield melts. To investigate the petrogenesis of the suite of glasses the REE patterns (Fig. S2) were fit to orthogonal polynomials using the method of O'Neill et al.¹² (Fig. 1). The coefficients of the polynomials, λ_n (where $\lambda_n = \lambda_0, \lambda_1$ and λ_2), parameterise the shape of a REE pattern in terms of the average REE abundance (λ_0), slope (λ_1) and curvature (λ_2). This approach enables subtle differences in patterns to be distinguished and quantified. For example, if curvature is plotted against slope, ocean floor basalts, Hawaiian shield tholeiites and melts from Loihi occupy well-defined characteristic fields, whereas the glasses of the basanite–nephelinite suite define a remarkable linear trend (Fig. 2). The λ_n of the glass REE patterns are given in Table S4.

Trends exhibited by the slope and curvature of REE patterns, such as that of the pre-shield basanite–nephelinite suite, can be

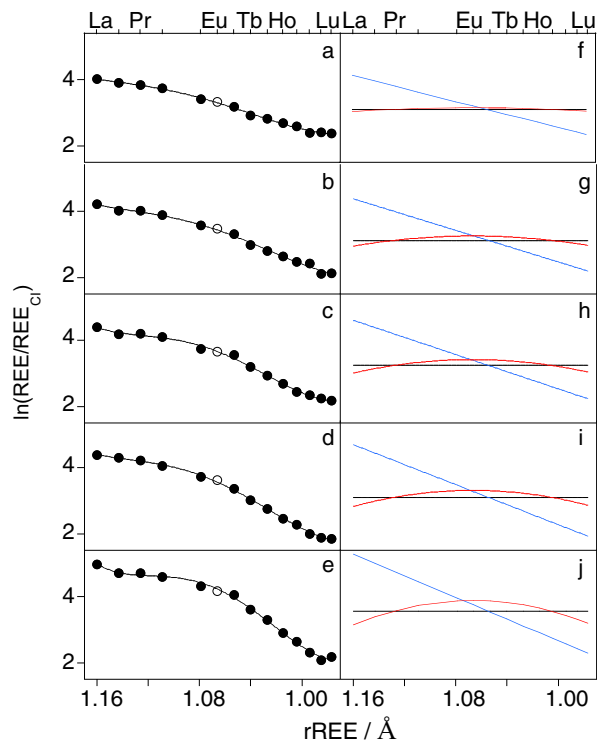


Fig. 1 Fits of the rare earth element (REE) patterns of the basanite–nephelinite suite to orthogonal polynomials. The chondrite normalised abundances of the REE (symbols) in **a** the least evolved glass (B11), **b** C13, **c** C18, **d** B20, and **e** the most evolved glass (C4), and the fits (Eq.1; black line) to the data resulting from the sum of the orthogonal polynomials shown in **f–j** where the value of the average REE abundance (λ_0 ; black) has been added to the orthogonal polynomials for slope ($\lambda_1 f_1$; blue) and curvature ($\lambda_2 f_2$; red) for ease of plotting. Eu was not included in the fits and is indicated by an open symbol in (**a–e**).

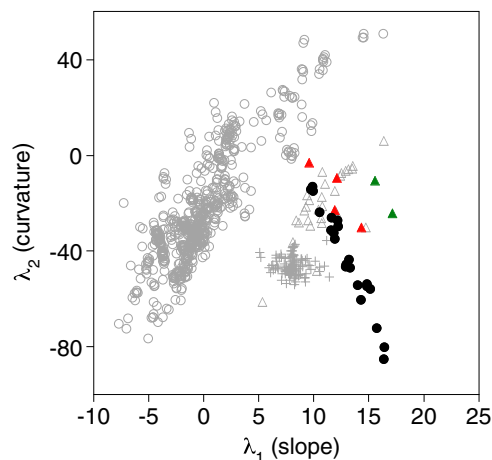


Fig. 2 The curvature (λ_2) and slope (λ_1) of the rare earth element (REE) patterns of basaltic melts. The λ_2 and λ_1 of the REE patterns of ocean floor basalts (open circles¹⁰), Hawaiian shield tholeiites (crosses¹³), melts from Loihi (triangles^{14,15}, including alkalic basalts (red) and basanites (green) for which fractionation of garnet has been suggested¹⁵), and the pre-shield Kilauean basanite–nephelinite glasses of this study (black).

modelled using the standard equations for partial melting and fractional crystallisation (e.g., Shaw¹⁶) and literature partition coefficients for common mantle minerals (garnet, clinopyroxene, orthopyroxene and olivine¹²). As garnet fractionates the REE

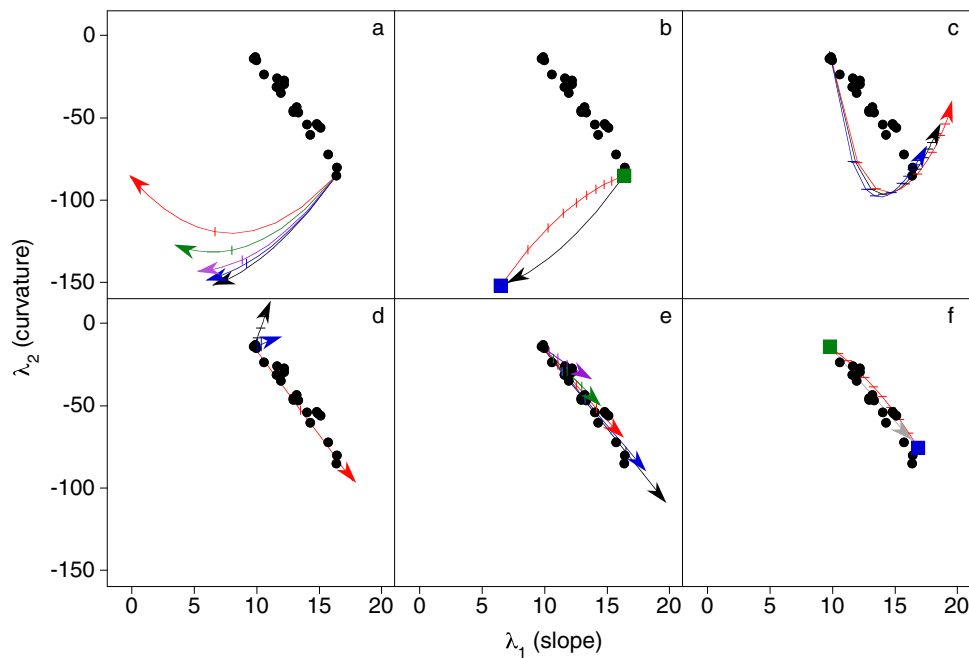


Fig. 3 Modelled trends in the curvature (λ_2) and slope (λ_1) of rare earth element (REE) patterns due to partial melting, fractional crystallisation, reactive melt flow and binary mixing. The λ_2 and λ_1 of the basanite-nephelinite glasses (black symbols) and trends in curvature and slope of the REE pattern of a melt due to **a** partial melting starting at the λ_1 λ_2 of the most evolved sample for 10% total melting (5% interval marked) where the relative proportions of clinopyroxene, orthopyroxene and olivine contributing to the melt are constant but the amount of garnet varies from 2 (black), 7 (blue), 14 (purple), 28 (green) to 50 (red) %, **b** linear mixing (red) of the most evolved sample (green square) and the melt (blue square) in **(a)** produced by 10% partial melting with 2% garnet (black vector), intervals of 10% are marked, **c** reactive flow of the least evolved melt flowing through a matrix of garnet peridotite with constant porosity (0.05; black), decreasing porosity (0.05–0.01; red) and increasing porosity (0.05–0.1; blue), intervals corresponding to a flow distance of 3, 7, 10% and then 10% increments to 80% are marked, **d** fractional crystallisation of 20% of garnet (red; i.e., 80% melt remaining), 40% clinopyroxene (blue) and 40% amphibole (black) from the least evolved sample, 10% intervals of crystallisation are marked, **e** fractional crystallisation of 40% garnet (gt) and clinopyroxene (cpx; i.e., 60% melt remaining) from the least evolved sample, where the fractionating assemblage varies from gt:cpx 0.5:0.5 (black), 0.4:0.6 (blue), 0.3:0.7 (red), 0.2:0.8 (green) to 0.1:0.9 (purple), 10% intervals of crystallisation are marked, and **f** linear mixing (red) of the least evolved sample (green square) and the residual melt (blue square) produced after that sample has undergone 42% fractional crystallisation of an assemblage consisting of 32% garnet 68% clinopyroxene (grey vector), 10% intervals of mixing are marked. Arrows show the direction of the petrogenetic processes.

more strongly than other mantle minerals it exerts the greatest control on the shape of a REE pattern and a range of models were produced by varying the amount of garnet melting or crystallising. The modelled slope and curvature trends are shown in Fig. 3, while the modelled average REE abundances, which are not as sensitive to different petrogenetic processes, are shown in Fig. S3. Partial melting was modelled to start at the slope and curvature of the most evolved sample and different models were produced by varying the amount of garnet contributing to the melt from 2 to 50% (Fig. 3a). The relative proportions of other contributing minerals were kept constant. Fractional crystallisation was modelled to start at the slope and curvature of the least evolved sample and different models were produced by varying the amount of garnet crystallising from 10 to 50% (Fig. 3d, e). Although, the proportion of garnet melting or crystallising is in some cases unrealistic they were modelled to illustrate the effect of garnet on REE pattern shape. Reactive melt flow, where a melt reacts with the matrix through which it is passing, can produce large enrichments in incompatible trace elements, similar to those exhibited by the present samples, and was also considered¹⁷. Models were produced for constant (0.05), increasing (0.05–0.1), and decreasing (0.05–0.01) matrix porosity with no mineralogical reaction, and for constant porosity and a mineralogical reaction of garnet peridotite to pyroxenite. The slope and curvature of the REE pattern of the first melt to flow through the matrix (i.e., the melt front) is shown in Fig. 3c and of

subsequent melt batches in Fig. S4. The melt front modelled for the mineralogical reaction is the same as the model for constant porosity as melt flow is required for the reaction and a difference between these models is only observed in subsequent melt batches (Fig. S4). All the models are described in detail in the Methods section. Significantly, fractional crystallisation, partial melting and reactive melt transport result in very different λ_n , with curved trends in slope and curvature for partial melting and reactive melt transport, though in opposing directions (Fig. 3a, c), and linear trends for fractional crystallisation (Fig. 3d, e). The REE patterns that correspond to these changes in slope and curvature are shown in Fig. S5.

At the low degrees of partial melting considered to produce alkalic melts (<10%¹⁸) the modelled trends proceed in a direction perpendicular to that defined by the slope and curvature of the glasses (Fig. 3a). Two co-genetic end-member melts formed by different degrees of partial melting would be connected by a partial melting trend such that binary mixing of these components would form a linear trend with a direction similar to that of the partial melting vectors (Fig. 3b). Thus, neither partial melting nor mixing of two end-member melts produced by partial melting of a common source can explain the observed changes in slope and curvature of the REE patterns.

Reactive melt flow produces curved trends in slope and curvature that also do not match the linear trend defined by the glasses (Fig. 3c; Fig. S4). The change in slope and curvature of the

melt fronts suggest reactive melt flow could produce a melt (e.g., at a flow distance of 30% for a model of constant porosity and no mineralogical reaction) that could mix with the original melt to form the series. However, the almost exponential increase predicted for incompatible trace elements (e.g., Fig. S3c) is not seen in the glasses, while it would also seem fortuitous that a melt produced at this particular flow distance formed binary mixing trend. Thus, as for partial melting, neither reactive melt flow nor binary mixing of an initial melt and a component produced by reactive melt flow can explain the changes in the REE patterns of the glasses.

The linear slope and curvature trend for the fractional crystallisation of garnet is identical to that of the glasses (Fig. 3d) suggesting that this process formed the melt suite. The crystallisation of garnet would decrease the average REE concentration of a melt (average REE garnet/melt partition coefficient, $D_{\text{REE}}^{\text{garnet/melt}} > 1$; Fig. S3b) and the relatively constant REE content of the glasses (λ_0 ; Table S4) suggests that another phase(s) with $D_{\text{REE}}^{\text{crystal/melt}} < 1$ must be crystallising alongside garnet. The crystallisation of clinopyroxene, amphibole, orthopyroxene, olivine, and phlogopite would have a negligible effect, relative to that of garnet, on the slope and curvature of the REE pattern of a residual melt (Fig. 3d). Indeed, the low compatibility of the REE in orthopyroxene, olivine and phlogopite means that the trends due to the crystallisation of these minerals are too small to be shown in Fig. 3d. The trends produced by clinopyroxene and amphibole have very different orientations to that of garnet, however, the relative magnitudes of the vectors means that the vector sum of garnet and clinopyroxene and/or amphibole would have almost the same direction as the garnet trend, such that the crystallisation of garnet masks the presence of other crystallising phases (Fig. 3e). Hence, while the average REE abundance (λ_0), slope (λ_1), and curvature (λ_2) of the glasses indicate that the suite was formed through fractional crystallisation involving garnet, little can be said about the other phase(s) also crystallising. Mixing of two cogenetic end-member melts that are related by fractional crystallisation involving garnet would produce a linear trend that is indistinguishable from the trend produced by garnet crystallisation (Fig. 3f). Although, in this case the petrogenetic implications of the two processes are the same as they both necessitate the crystallisation of garnet.

The minerals that would crystallise from the least evolved composition (B11) were determined by experiments from 3 to 5 GPa and 1300–1450 °C. Garnet was identified as a liquidus phase in the highest pressure experiment (Fig. S6), while clinopyroxene crystallised at all pressures (Table S5a). The garnet crystals have atomic $\text{Ca}/(\text{Ca}+\text{M}) \sim 0.4$, where $\text{M} = \text{Mg} + \text{Fe} + \text{Mn}$, which is typical of eclogitic¹⁹ and distinct from peridotitic garnets, where $\text{Ca}/(\text{Ca}+\text{M})$ is buffered to lower values by the presence of orthopyroxene (~ 0.13 ²⁰). The jadeite component of the clinopyroxene is ~ 0.3 , which is similar to that of the eclogitic pyroxene omphacite. Therefore, the experiments suggest that the least evolved composition would fractionate an assemblage with an eclogitic composition.

The generation of the suite was further explored by calculating the bulk crystal/melt partition coefficients ($D_{\text{M}}^{\text{crystal/melt}}$) of the trace elements (M). The two most evolved glasses were excluded from this calculation, and also from the derivation of the cotectic assemblage that follows, as they show marked increases or decreases in the concentrations of some elements relative to the other glasses of the suite (e.g., Ni, FeO; Tables S1, S2; see “Methods”). To determine $D_{\text{M}}^{\text{crystal/melt}}$ the trace element contents of the glasses were fit to the equation for fractional crystallisation by least squares regression (see “Methods”). The resulting $D_{\text{M}}^{\text{crystal/melt}}$ are given in Table S6, and the degrees of

crystallisation required to produce each glass from the least evolved composition (B11), which is a subsidiary result of the calculation, are given in Table S4. The glasses are related by a total of 40% fractional crystallisation (i.e., 60% residual melt), while the $D_{\text{M}}^{\text{crystal/melt}}$ are generally consistent with a fractionating assemblage of garnet and clinopyroxene²¹ (Fig. S7). The high CO_2 contents of the glasses (Table S1) indicate that they were erupted at a water-column pressure sufficient to prevent complete degassing of CO_2 . As CO_2 is preferentially fractionated into vapour with respect to H_2O ²² the relatively high partition coefficient of H_2O (0.57; Table S6) can be attributed to moderately compatible behaviour rather than degassing. This suggests that a hydrous phase such as phlogopite or pargasite was also part of the fractionating assemblage. Phlogopite is stable at higher pressures than pargasite^{23,24}, which in addition to the moderately compatible behaviour of Rb and Ba (Table S6²⁵), indicates that phlogopite is more likely. Phlogopite was not crystallised experimentally since the experiments were nominally anhydrous. Cr has a particularly high partition coefficient suggesting Cr-rich garnet or clinopyroxene.

The REE pattern shape coefficients and trace element bulk partition coefficients indicate that the suite was formed by the crystallisation of garnet, clinopyroxene and phlogopite. Thus, the changes in major element concentrations, which represent the bulk fractionating composition, were decomposed into these mineral components using least squares regression (see “Methods”). The best fit to the composition was an assemblage of clinopyroxene (63%), garnet (32%), and phlogopite (5%), using a stoichiometric composition for phlogopite and the experimentally determined compositions of clinopyroxene and garnet (Table S5b). The agreement between the measured and modelled major element compositions is illustrated for MgO and Na_2O , as a function of the degree of crystallisation determined from the trace element data, in Fig. 4.

The consistency between the REE shape modelling, the compositions determined experimentally, the modelled partition coefficients, and the modelled cotectic assemblage identify fractional crystallisation as the process by which the suite of glasses was formed. An alternative method of parameterising REE shape, using Dy/Yb to approximate the slope and Dy/Dy^* , where Dy^* is the value for Dy obtained by linear interpolation between La and Yb, to approximate the curvature, similarly indicates that the glass suite was formed through the fractional crystallisation of garnet (Fig. S8; see Fig. 4d in Davidson et al.²⁶). The proportion of garnet crystallising (32% of the fractionating assemblage) and

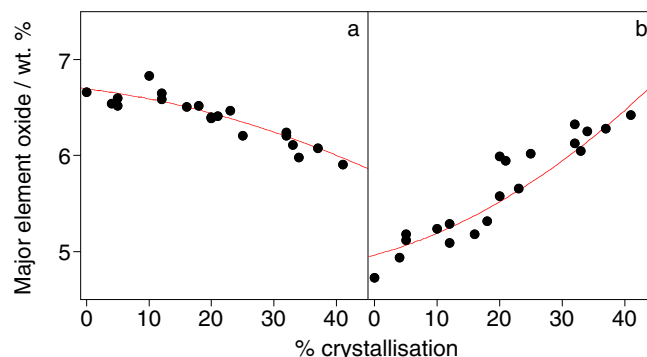


Fig. 4 Major element contents of the basanite-nephelinite suite.

Measured (black) and predicted (for a fractionating assemblage of clinopyroxene (63%), garnet (32%), and phlogopite (5%); red) **a** MgO and **b** Na_2O contents of the glasses versus the degree of crystallisation determined from fitting the trace element contents to the equation for fractional crystallisation (Eq. 12).

the degree of crystallisation (40%) were determined by models independent of the REE shape modelling. Yet the predicted change in REE pattern slope and curvature for 40% crystallisation with garnet forming ~32% of the fractionating assemblage is an extraordinarily close match to the trend in slope and curvature of the suite of glasses (red trend; Fig. 3e; with the two most evolved glasses excluded as these were not included in the modelling).

Fractional crystallisation beneath pre-shield Kilauea. The fractionation of garnet from primitive mantle melts was shown to produce alkalic melts by early experimental studies^{27,28}. However, this process fell out of favour as later work showed that varying degrees of partial melting could generate the range of alkalic melts seen at Hawaii²⁹. Indeed, the basanite-nephelinite suite of the present study was attributed to varying degrees of partial melting of a garnet lherzolite source⁸. However, modelling of the REE patterns unambiguously shows that the suite was formed by fractional crystallisation rather than partial melting (Fig. 3). More recently, it has been shown that orthopyroxene and garnet can crystallise at the expense of olivine from a carbonated silicate melt to produce nephelinite and basanite compositions³⁰. The fractional crystallisation of eclogite from alkalic melts has also been proposed previously³¹ but not, to our knowledge, for Hawaiian pre-shield melts.

The development of relatively deep (<30 km) ephemeral magma chambers in the early stages of intraplate oceanic volcanoes is well documented^{2,32–34}, where low melt flux results in deep storage³⁵. Melts erupted by these young volcanoes can be the products of extensive fractionation as they stall in the cold lithosphere before establishing an open conduit to the surface. The formation of the pre-shield suite of glasses by fractional crystallisation suggests that a magma chamber (this term is used here without implications for size, shape or longevity) similarly formed during the birth of Kilauea. Garnet occurs on the liquidus of the least evolved composition at 5 GPa (~150 km), however, as the experiments may not exactly replicate natural conditions these results do not necessarily suggest a magma chamber at 150 km. There is a strong association between alkalic melts and carbonated sources³⁶ and the presence of CO₂ increases the stability field of garnet, with garnet being present on the liquidus of carbonated basanite/nephelinite (>2.6 wt.% CO₂) melts at pressures as low as 3 GPa (90 km³⁰). The CO₂ contents of the present glasses (up to 0.8 wt.%; Table S1) may not be representative of their original contents as they could have experienced degassing. Seismic studies indicate that the lithosphere beneath Hawaii extends to ~110 km³⁷ and has some rigidity to ~150 km³⁸, while the thickness of old oceanic lithosphere, which the leading edge of the Hawaiian hotspot would encounter, is ~100 km^{37,38}. Melt is considered to be generated at depths 90–120 km beneath Kilauea^{4,39} with earthquake foci tracking magma transport from depths > 50 km^{40,41}. Rare garnet pyroxenite xenoliths erupted by rejuvenated volcanism at Oahu are considered to be accumulates that originated at depths between 60 and 90 km (Bizimis et al.⁴² and references therein), further indicating stable lithosphere deep beneath Hawaii.

The seismic and petrological evidence suggest that a deep magma chamber is possible, with the stability of garnet in the experiments of Mallik and Dasgupta³⁰ placing an upper limit on the depth. This depth (>90 km) is, however, strikingly deeper than that invoked for other oceanic intraplate volcanoes (< 30 km³⁴). Hawaii has often been considered the archetype of hotspot volcanism, although as the buoyancy flux is at least twice that of others⁴³ (apart from Iceland) it is more likely to be the exception. The development of an unusually deep pre-shield

magma chamber is therefore perhaps in keeping with the atypical character of Hawaii. Alkalic pre-shield melts at Loihi that are thought to have been differentiated by the fractionation of garnet¹⁵ show a similar linear trend between the curvature and slope of the REE patterns as observed for the glasses studied here (Fig. 2). This suggests that deep fractional crystallisation may have also played a role in the genesis of melts erupted by Loihi and could be a general process for young Hawaiian volcanoes.

Both fractional crystallisation and partial melting play important roles in the generation of alkalic melts. Here we demonstrate unambiguously the role of garnet crystallisation in the formation of pre-shield stage Hawaiian melts. This challenges the viewpoint that fractional crystallisation is solely a shallow process and suggests that the development of a deep (> 90 km) magma chamber is an important early stage in the birth of a Hawaiian volcano.

Methods

Experimental. A synthetic version of the least evolved glass (B11) was prepared using powders of reagent grade oxides, carbonates, and synthetic fayalite. The oxide and carbonate powders were dried prior to weighing. All of the components were mixed under acetone using an agate pestle and mortar for ~20 min. The mixture was pressed into a pellet and de-carbonated at 1000 °C for > 12 h. The pellet was then crushed and ground for ~30 min under acetone. The resulting powder was equilibrated over a range of temperatures (1300–1450 °C) and pressures (3–5 GPa) for 24 h, in graphite capsules, using MgO-pyrex-NaCl assemblies, and an end-loaded piston-cylinder apparatus. Each capsule was mounted in epoxy resin and ground back to expose the sample, which was then polished.

Analytical. A JEOL 8530F electron probe microanalyser (EPMA) operating at 15 kV and 80 nA, with a spot size of 10 μm, was used to determine the major element compositions of the natural glasses. The EPMA was calibrated using Astimex Standards Ltd mineral standards and VG2 for S. The major element compositions determined in this study and in Sisson et al.⁸ agree within 3%, other than Na₂O and MnO, which are within 6 and 8%, respectively. There is a large difference between the S contents of the two studies, which is attributed to differences in the S content assumed for VG2 (1200 ± 80 ppm in Coombs et al.⁴⁴ and 1420 ppm here; see O'Neill⁴⁵ for a compilation). The natural glasses and experimental samples were examined using a JEOL 6400 scanning electron microscope operating at 15 kV. Back-scattered electron (BSE) images were used to determine the proportion of phases in the experimental samples by counting the pixels of the grey-scale associated with each phase (e.g., the garnet crystals are pale grey; Fig. S6) and dividing by the total pixels in the image. The compositions of the synthetic glasses and crystals were determined using energy dispersive spectroscopy. The phase equilibrium assemblages and the average compositions of the crystals are given in Tables S5a and S5b.

Attenuated total reflectance Fourier transform infra-red (ATR-FTIR) spectra were recorded from the natural glasses using a Ge ATR crystal with a refractive index of 4.0, a Hyperion infrared microscope, and a Bruker Tensor 27 spectrometer equipped with a KBr beamsplitter and liquid N₂ cooled DTGS detector. The chamber was purged with dry air prior to and during acquisition of the spectra and a background was recorded after every six spectra. The infra-red spot size was 10 μm and the penetration depth ~1 μm. Spectra were recorded from 650 to 5000 cm⁻¹ with a spectral resolution of 4 cm⁻¹. Synthetic mid-ocean ridge basalt (MORB) glasses with known H₂O contents were used as standards⁴⁶. Three replicate spectra were recorded for all samples and standards. For each spectrum the area of the O–H band between 3100 and 3750 cm⁻¹ was normalised to that of the silicate band between 810 and 850 cm⁻¹ and the H₂O contents determined using a calibration based on the standards⁴⁷. The average difference between the water contents determined for the standards and the published values was 0.11 wt.%. Low intensity peaks at 1410 and 1501 cm⁻¹ observed in some of the spectra were assigned to vibrations of CO₃²⁻ in the glasses⁴⁸ and used to determine the concentration of CO₂⁴⁹. The H₂O and CO₂ contents of the glasses are given in Table S1. The CO₂ contents have a logarithmic relationship with the total alkali content (Fig. S9), in contrast to the linear relationship predicted for CO₂ solubility²², but in keeping with a reciprocal solution model proposed for S²⁻⁴⁵. If this model is appropriate for CO₂, the correlation suggests degassing at constant pressure with the different CO₂ contents being controlled by composition.

The trace element concentrations of the natural glasses were determined by laser ablation inductively coupled plasma mass spectrometry, LA-ICP-MS, using analytical protocols and standards similar to those of Jenner and O'Neill⁵⁰. The instrument comprises a 193 nm wavelength ArF EXCIMER laser coupled to an Agilent 7500S quadrupole ICP-MS. The diameter of the analysis spot was 28 μm. The acquisition time per analysis was 70 s, with the first and last 20 s recorded as background before and after ablation. Glass analyses were obtained in batches of up to nine, bracketed before and after by analyses of standards. The trace element

concentrations were determined using two routines. The first routine comprised the elements reported by Sisson et al.⁸ (²⁹Si, ⁴³Ca, ⁸⁵Rb, ⁸⁸Sr, ⁸⁹Y, ⁹⁰Zr, ⁹³Nb, ¹³⁸Ba, the REE, ¹⁷⁷Hf, ¹⁸¹Ta, ²⁰⁷Pb, ²³²Th, ²³⁸U) and was recorded for glasses not analysed in that study (B11, B10, B19, and B20). The second routine comprised ⁷Li, ⁹Be, ²⁹Si, ⁴³Ca, ⁴⁵Sc, ⁵¹V, ⁵³Cr, ⁵⁵Mn, ⁵⁹Co, ⁶⁰Ni, ⁶⁵Cu, ⁶⁶Zn, ⁷¹Ga, ⁹⁵Mo, ¹¹⁸Sn, and ²⁰⁵Tl, and was recorded for all of the glasses for which there was space for a laser spot. Replicate analyses were recorded where possible. NIST 612 was used as an external standard, and NIST 610 and BCR-2G as secondary standards. The Ca content of the glasses determined by EPMA and the count rate of ⁴³Ca was used as the internal standard. The Python package LAtools was used for data reduction^{9,51}. The LA-ICP-MS analyses of the standards have a precision, defined by the relative standard deviation, of < 5%, except for Tl, which is 10%. The LA-ICP-MS results from this study are given in Table S2, together with data from Sisson et al.⁸ for glasses where new analyses were not possible. There appears to be a systematic offset (~10%) between the results of the two studies based upon differences in the smooth trends between trace elements and total alkali content. This offset is attributed to differences in the standards or data reduction methods.

λ_n fitting. The geochemical behaviour of most of the REE is controlled by the decrease in ionic radius with increasing atomic number for constant charge (3+). Consequently, the abundances of the REE in a melt vary as a function of their radii (r_{REE}) and the resulting REE pattern can be fit to orthogonal polynomials that are derived from the radii¹². The obvious exceptions to this are Ce and Eu, which can occur as Ce⁴⁺ and Eu²⁺, and these REE should be excluded from the fit if Ce⁴⁺ and/or Eu²⁺ are present. Orthogonal polynomials are used to ensure that the coefficients of the polynomials vary independently of each other, although this is only strictly true if the same number of REE are used in the fit as were used to derive the polynomials. The orthogonal polynomials used here (given in Tables 1 and 2 of O'Neill¹²) were derived from the radii of the same 13 REE fit in the present study (Eu was excluded as it commonly occurs as Eu²⁺ in basalts). The fit of the orthogonal polynomials to a REE pattern can be written as:

$$\ln([\text{REE}]/[\text{REE}]_{\text{CI}}) = \lambda_0 f_0^{\text{orth}} + \lambda_1 f_1^{\text{orth}} + \lambda_2 f_2^{\text{orth}} + \lambda_3 f_3^{\text{orth}} + \lambda_4 f_4^{\text{orth}} + \text{etc.}, \quad (1)$$

where $[\text{REE}]/[\text{REE}]_{\text{CI}}$ refers to the chondrite (CI) normalised REE abundances, f_n^{orth} to the orthogonal polynomials and λ_n to the coefficients of the orthogonal polynomials, where n is the order of the polynomial. Higher order functions than f_2^{orth} commonly reflect nothing more than 'noise'¹². The manner in which the coefficients and polynomials describe the shape of a REE pattern is illustrated by example fits shown in Fig. 1. The orthogonal polynomials describe different shape components: f_0^{orth} is a constant function (black line in Fig. 1f–j), f_1^{orth} a linear function (blue line in Fig. 1f–j), and f_2^{orth} a quadratic function (red line in Fig. 1f–j). The coefficients parameterise the contribution of each polynomial to the REE pattern shape: λ_0 is the average REE concentration of the pattern (i.e., the y intercept of the constant function; $\lambda_0 = 3.10$ in Fig. 1f and $\lambda_0 = 3.56$ in Fig. 1j), λ_1 the slope of the REE pattern (i.e., the gradient of the linear function; $\lambda_1 = 9.75$ in Fig. 1f and $\lambda_1 = 16.34$ in Fig. 1j), and λ_2 the curvature of the REE pattern (i.e., the openness or tightness and upward or downward opening of the quadratic function; $\lambda_2 = -14.1$ in Fig. 1f and $\lambda_2 = -85.1$ in Fig. 1j). The shape coefficients, λ_n , were calculated for the REE patterns of the glasses. The λ_n are given in Table S4.

λ_n modelling. The partition coefficients, $D_{\text{M}}^{\text{crystal/melt}}$ where M is an element, of the REE are smooth functions of r_{REE} and can be fit to the orthogonal polynomials in the same way as the REE patterns:

$$D_{\text{REE}}^{\text{crystal/melt}} = \delta_0 f_0^{\text{orth}} + \delta_1 f_1^{\text{orth}} + \delta_2 f_2^{\text{orth}} + \delta_3 f_3^{\text{orth}} + \delta_4 f_4^{\text{orth}} + \text{etc.}, \quad (2)$$

where the δ_n coefficients describe the shape of the REE partitioning pattern (in the same way as λ_n describes the shape of a REE pattern). The right hand side of Eq. 2 can then be substituted for $D_{\text{REE}}^{\text{crystal/melt}}$ in models of petrogenetic processes.

Models of fractional crystallisation were constructed using the equation:¹⁶

$$[M]/[M_0] = F^{D-1} \quad (3)$$

which rearranges to:

$$\ln([M]/[M_0]) = \ln(F)(D_M - 1) \quad (4)$$

where $[M]$ is the concentration of element M in the melt, $[M_0]$ the initial concentration, F the mass fraction of melt (which varies between 0 and 1, where 1 is zero crystallisation) and D_M the bulk partition coefficient, $\Sigma D_{\text{M}}^{\text{crystal/melt}} m_x$, where m_x is the mass fraction of the crystalline phase x . Combining Eq. 2 with Eq. 4 gives:

$$\psi_0 = \ln(F)(\Sigma m_x \delta_0 - 1), \psi_1 = \ln(F)(\Sigma m_x \delta_1) \text{ and } \psi_2 = \ln(F)(\Sigma m_x \delta_2) \quad (5)$$

where ψ_0 , ψ_1 , and ψ_2 are termed petrogenetic process vectors, which describe the change in average REE abundance (ψ_0), slope (ψ_1) and curvature (ψ_2) between the initial and observed REE patterns. The change in REE pattern shape can also be determined by using Eq. 3 to generate multiple REE patterns as a function of the degree of crystallisation (F). These REE patterns could then be fit to the orthogonal polynomials to quantify the differences between patterns, or change in λ_n (Ψ_n), due

to fractional crystallisation. However, this method is time consuming as it requires fitting many REE patterns to the orthogonal polynomials rather than a single fit to the partition coefficients.

The partial melting models were constructed using the equation for batch melting:¹⁶

$$[M]/[M_0] = 1/[D_0 + F(1 - P)] \quad (6)$$

or

$$\ln([M]/[M_0]) = -\ln(D_0 - FP + F) \quad (7)$$

where F is the mass fraction of melt, D_0 the initial bulk partition coefficient given by $\Sigma D_{\text{M}}^{\text{crystal/melt}} m_x^0$, where m_x^0 is the mass fraction of the crystalline phase x in the source, and P the bulk distribution coefficient for the melting assemblage of minerals given by $\Sigma D_{\text{M}}^{\text{crystal/melt}} p_x$, where p_x is the mass fraction of the crystalline phase x entering the melt. It is not possible to construct simple petrogenetic process vectors (Ψ_n) for this equation. As a result Eq. 6 was used to determine the amounts of each REE, and hence the REE patterns, as a function of F , which were then fit to the orthogonal polynomials (Eq. 1). The change in pattern shape as a function of F could then be determined.

The effects of fractional crystallisation and partial melting on REE pattern shape were modelled using the methodology described above (worked examples of both processes are included as an excel spreadsheet in the supplementary information; Worked Example 1). The shapes of the REE mineral/melt partition coefficient patterns (as parameterised by δ_n) used in the models are from Table 7 in O'Neill¹². It is the relative difference between the $D_{\text{REE}}^{\text{crystal/melt}}$ (i.e., the pattern shape) that is important for defining the direction of a process in lambda space (e.g., the fractional crystallisation vectors in Fig. 3d), with the absolute values of D defining the magnitude of the change (e.g., the length of the vectors in Fig. 3d). This means that vectors for the different mantle minerals have very different directions (Fig. 3d), but the vectors for a particular mineral (generated using different $D_{\text{REE}}^{\text{crystal/melt}}$) all have a similar direction. Thus, the values of $D_{\text{REE}}^{\text{crystal/melt}}$ used in the models, within the typical ranges, make little difference to the direction of the mineral vectors.

Fractional crystallisation was modelled to start from the least evolved glass (B11; Fig. 3d,e), and partial melting from the most evolved glass (C4; Fig. 3a). In both cases, these are melt compositions rather than source compositions. These starting points were chosen to facilitate direct comparison with the basanite-nephelinite λ_n . The proportion of garnet melting (Fig. 3a) and crystallising (Fig. 3e) was varied in the models. Relative to garnet and clinopyroxene, the REE have lower compatibilities in other common mantle minerals (i.e., orthopyroxene, olivine, and spinel) meaning that these minerals could be omitted from models of fractional crystallisation (Fig. 3e).

Reactive melt flow was modelled following the incremental method of Reiners¹⁷. In this approach the matrix or column through which the melt flows is divided into a series of cells, where it takes the melt one time step (j) to advance through one cell (i). The concentration of an element (C) is determined in each cell for each timestep for a sequence of cells (0 to i) and time steps (0 to j):

$$C_i^j = \frac{\rho_f \phi_{i-1}^{j-1} C_{i-1}^{j-1} + \rho_s (1 - \phi_i^{j-1}) C_s^{j-1}}{\rho_f \phi_i^j + \rho_s (1 - \phi_i^j) D_{\text{Mi}}^j} \quad (8)$$

where C_i is the initial concentration of the element in the melt, ρ_f the density of the melt, C_s the initial concentration of the element in the matrix, ρ_s the density of the matrix, ϕ the porosity of the matrix and $D_{\text{M}}^{\text{crystal/melt}}$ the crystal melt partition coefficients. As the melt moves it remains in local equilibrium with the matrix such that:

$$C_{si}^j = C_{fi}^j (D_i^j) \quad (9)$$

In models of changing porosity, from an initial value ϕ_0 to a final value ϕ_1 , a rate of change (r) of 0.05 per cell was used. To conserve mass within a column ϕ was changed at a uniform rate for all cells at each time step such that $\phi = \phi_0$ when $j = 0$, and in subsequent time steps:

$$\phi^j = \phi^{j-1} + r(\phi_1) - \phi^{j-1} \quad (10)$$

The change in partition coefficient due to a mineralogical reaction, from an initial value (D_{M}^0) for the original mineral assemblage (e.g., garnet peridotite) to a final value (D_{M}^1) for the resultant assemblage (e.g., pyroxenite), was modelled using the same rate of change. The D_{M} of the melt front is D_{M}^0 and for subsequent melt batches is given by:

$$D_{\text{M}}^j = D_{\text{M}}^{j-1} + r(D_{\text{M}}^1 - D_{\text{M}}^{j-1}) \quad (11)$$

Reactive melt flow models used an input melt with the composition of the least evolved glass (B11), a garnet peridotite matrix, $\rho_f = 2800 \text{ kg/m}^3$, $\rho_s = 3300 \text{ kg/m}^3$ and $\phi_0 = 0.05$. In models of decreasing and increasing porosity ϕ_1 was 0.01 and 0.1 respectively. In a model of changing matrix mineralogy D_{M} were changed from those of a garnet peridotite (D_{M}^0) to those of a pyroxenite (D_{M}^1), where the D_{M} were calculated from the mineral-melt partition coefficients for the reaction 65% olivine + 24% clinopyroxene + 6% orthopyroxene + 5% garnet = 10% olivine + 75% clinopyroxene + 15% garnet. The column through which the melt flows was divided into 30 cells and the concentration of each REE was calculated using Eq. 8 to Eq. 11 for each cell for $i = 0$ to 30 and $j = 0$ to 120. Each cell was assigned a

length of 100 m and the time taken for the melt to flow through a single cell was 20 y. The time taken for the melt to flow through one column (3000 m) is thus 600 y. The values of these parameters (ρ_B , ρ_S , ϕ , ϕ^1 , D_M , D_M^1 cell size and melt flow rate) were taken from Reiners¹⁷. A worked example is included as an excel spreadsheet in the supplementary information (Worked Example 2). The REE patterns of the melt front and of subsequent melts at discrete time intervals were fit to orthogonal polynomials¹² to parameterise the shape of the patterns. The change in REE pattern shape due to reactive melt flow was then determined.

Trace element bulk crystal-melt partition coefficients and the degree of crystallisation. To determine the bulk partition coefficient (D_M) of each element (M) and the degree of crystallisation (F) for each glass the concentration of each trace element in each sample (n_s) was fit to the equation for fractional crystallisation (Eq. 3) in the form:

$$\ln[M_{(\text{calc})}] = [\ln M_0] + \ln F(D_M - 1) \quad (12)$$

where $[M_{(\text{calc})}]$ is the calculated concentration of element M and $[M_0]$ the calculated initial concentration (equivalent to the modelled concentration of the least evolved melt, B11). The problem was solved by minimising χ^2 defined as:

$$\chi^2 = \sum M \sum n_s (\ln[M_{\text{mes}} * f_M] - \ln[M_{(\text{calc})}])^2 / \sigma(\ln M)^2 \quad (13)$$

where $[M_{\text{mes}}]$ are the measured trace element contents of the glasses (Table S2) and $\sigma(\ln M)^2$ are taken to be 5% for all the elements except Ti, for which it is 10%. In order to reconcile the data of Sisson et al.⁸ with the new analytical results reported here a correction factor, f_M , was included and refined for each element that was analysed in both this study and Sisson et al.⁸. Due to the large disparity between the Pb contents determined in the two studies this element was excluded from the fit. The value of F was set to 1 (i.e., zero crystallisation) for the least evolved sample. While the entire set of glasses form a continuous series in terms of REE the two most evolved glasses (A13 and C4) have anomalous concentrations, relative to the trends defined by the other samples, of some major and trace elements, which are attributed to the presence of an additional fractionating phase (possibly a Fe-Ti oxide). These two glasses were excluded from the fit. For 20 samples and 39 elements, there are 668 observations (allowing for some missing data) and 120 parameters to be refined (F , f_M , M_0 , D_M), giving 548 degrees of freedom. However, the problem is ill-posed due to the high degree of correlation between F and D_M , where changes in F are compensated by changes in D_M with insignificant changes to the minimised χ^2 . Nevertheless, the relative magnitudes of the calculated F and D_M remain the same and the most incompatible elements are always Be, La, Ce, Ti, and Th. The model was therefore constrained by setting D_{Th} to 0; Th was chosen as it is better determined than Be and Ti, and is independent of the REE modelling. The reduced χ^2 for the resulting regression is 1.8 indicating that the data are well fit by the model given the assessed uncertainties used in the weighting. The predicted values of D_M are given in Table S6 and the degree of crystallisation calculated for each glass in Table S4.

Cotectic assemblage. The REE shape modelling indicates the cotectic crystallisation of garnet and clinopyroxene. To model the cotectic mineral assemblage the bulk cotectic composition needs to be first determined. The good fit of the trace element data to a model of fractional crystallisation suggests that an assumption of constant values of D_M is not unreasonable. This in turn suggests that the crystallising assemblage did not change significantly during the evolution of the suite. Using this assumption, the values of F from the trace element modelling may be used to determine the bulk cotectic composition from a mass balance calculation for each major element oxide component, y :

$$[M_{y(\text{calc})}] = ([M_{y0}] - [M_{y(\text{cotectic})}](1 - F))/F \quad (14)$$

where $[M_{y(\text{cotectic})}]$ is the concentration of y in the cotectic composition, $[M_{y0}]$ the calculated starting composition of the least evolved glass, and $[M_{y(\text{calc})}]$ the calculated composition of each glass. The problem was solved by minimising χ^2 defined as:

$$\chi^2 = \sum y \sum n_s ([M_{y(\text{mes})}] - [M_{y(\text{calc})}])^2 / \sigma(y)^2 \quad (15)$$

where $[M_{y(\text{mes})}]$ is the measured concentration of each major element oxide component (Table S1), n_s the sample, and $\sigma(y)$ the uncertainty, which varied according to the uncertainty of the EPMA analyses. The constraint $\sum M_{y(\text{cotectic})} = 100$ (wt. %) was imposed during fitting. The bulk cotectic composition determined was 48 wt. % SiO₂, 1 wt. % TiO₂, 18 wt. % Al₂O₃, 0.2 wt. % MnO, 8 wt. % MgO, 12 wt. % CaO, 2.5 wt. % Na₂O, 0.5 wt. % K₂O and 10 wt. % FeO. The reduced χ^2 for the regression was 1.1.

The bulk composition of the cotectic can then be used to determine the proportions of the cotectic phases. The calculation was carried out in cation fractions, conflating Mg, Fe²⁺, and Mn together as one cation component, since these cations substitute freely for each other in the relevant phases. The composition was decomposed by least-squares regression into the experimentally determined garnet and clinopyroxene compositions (Table S5b) plus ideal end-member phlogopite. The best fit composition was clinopyroxene (63%), garnet (32%), and phlogopite (5%), for which the largest errors were for SiO₂ (2% excess) and CaO (4% deficit).

Data availability

All data generated or analysed in this study are provided in the Supplementary Information. Source data are provided with this paper.

Received: 16 September 2021; Accepted: 6 April 2022;

Published online: 26 May 2022

References

- Clague, D. A. & Dalrymple, G. B. *Volcanism in Hawaii* Vol. 1 (eds Decker, R. W., Wright, T. L. & Stauffer, P. H.) 5–54 (US Geological Survey Professional Paper, 1987).
- Clague, D. A. & Dixon, J. E. Extrinsic controls on the evolution of Hawaiian ocean island volcanoes. *Geochem., Geophys., Geosyst.* **1**, 1010 (2000).
- Kimura, J. I., Sisson, T. W., Nakano, N., Coombs, M. L. & Lipman, P. W. Isotope geochemistry of early Kilauea magmas from the submarine Hilina bench: The nature of the Hilina mantle component. *J. Volcanol. Geotherm. Res.* **151**, 51–72 (2006).
- Rhodes, J. M. The aluminum conundrum in Hawaiian shield-building lavas: An argument for a deep, garnet-bearing, mantle source. *Geochim. Cosmochim. Acta* **185**, 216–231 (2016).
- Frey, F. A., Garcia, M. O., Wise, W. S., Kennedy, A., Gurriet, P. & Albarede, F. The evolution of Mauna Kea volcano, Hawaii: petrogenesis of tholeiitic and alkalic basalts. *J. Geophys. Res.: Solid Earth* **96**, 14347–14375 (1991).
- Coombs, M. L., Sisson, T. W. & Lipman, P. W. Growth history of Kilauea inferred from volatile concentrations in submarine-collected basalts. *J. Volcanol. Geotherm. Res.* **151**, 19–49 (2006).
- Lipman, P. W., Sisson, T. W., Ui, T., Naka, J. & Smith, J. R. Ancestral submarine growth of Kilauea volcano and instability of its south flank. (eds Takahashi, E., Lipman, P. W., Garcia, M. O., Naka, J. & Aranaki, S.) 128, 161–191 (Deep Underwater Perspectives, American Geophysical Union, Hawaiian Volcanoes, 2002).
- Sisson, T. W., Kimura, J. I. & Coombs, M. L. Basanite-nephelinite suite from early Kilauea: carbonated melts of phlogopite-garnet peridotite at Hawaii's leading magmatic edge. *Contributions Mineral. Petrol.* **158**, 803–829 (2009).
- Palme, H. & O'Neill, H. St. C. Cosmochemical estimates of mantle composition. In *Treatise on Geochemistry* 2nd edn, Vol. 3 (eds Holland, H. D. & Turekian, K. K.) 1–39 (Elsevier, 2014).
- Jenner, F. E. & O'Neill, H. St. C. Analysis of 60 elements in 616 ocean floor basaltic glasses. *Geochem., Geophys., Geosyst.* **13**, GC004009 (2012).
- Yang, H. J., Frey, F. A. & Clague, D. A. Constraints on the source components of lavas from the Hawaiian North Arch and Honolulu volcanics. *J. Petrol.* **44**, 603–627 (2003).
- O'Neill, H. St. C. The smoothness and shapes of chondrite-normalized rare earth element patterns in basalts. *J. Petrol.* **57**, 1463–1508 (2016).
- Feigenson, M. D., Bolge, L. L., Carr, M. J. & Herzburg, C. T. REE inverse modeling of HSDP2 basalts: Evidence for multiple sources in the Hawaiian plume. *Geochem., Geophys., Geosyst.* **4**, 8706 (2003).
- Garcia, M. O., Foss, D. J. P., West, H. B. & Mahoney, J. J. Geochemical and isotopic evolution of Loihi Volcano, Hawaii. *J. Petrol.* **36**, 1647–1674 (1995).
- Frey, F. A. & Clague, D. A. Geochemistry of diverse basalt types from Loihi Seamount, Hawaii: Petrogenetic implications. *Earth Planet. Sci. Lett.* **66**, 337–355 (1983).
- Shaw, D. *Trace Elements in Magmas: A Theoretical Treatment* (Cambridge University Press, 2006).
- Reiners, P. W. Reactive melt transport in the mantle and geochemical signatures of mantle-derived magmas. *J. Petrol.* **39**, 1039–1061 (1998).
- Clague, D. A. & Frey, F. A. Petrology and trace element geochemistry of the Honolulu Volcanics, Oahu: Implications for the oceanic mantle below Hawaii. *J. Petrol.* **23**, 447–504 (1982).
- Coleman, R. G., Lee, D. E., Beatty, L. B. & Brannock, W. W. Eclogites and eclogites: Their differences and similarities. *Geol. Soc. Am. Bull.* **76**, 483–508 (1965).
- Klemme, S. & O'Neill, H. St. C. The near-solidus transition from garnet lherzolite to spinel lherzolite. *Contributions Mineral. Petrol.* **138**, 237–248 (2000).
- Adam, J. & Green, T. Trace element partitioning between mica- and amphibole-bearing garnet lherzolite and hydrous basanitic melt: 1. Experimental results and the investigation of controls on partitioning behaviour. *Contributions Mineral. Petrol.* **152**, 1–17 (2006).
- Dixon, J. E. Degassing of alkalic basalts. *Am. Mineralogist* **82**, 368–378 (1997).
- Green, D. H., Hibberson, W. O., Kovacs, I. & Rosenthal, A. Water and its influence on the lithosphere-asthenosphere boundary. *Nature* **467**, 448–451 (2010).
- Frost, D. J. The stability of hydrous mantle phases. *Rev. Mineral. Geochem.* **62**, 243–271 (2006).

25. La Tourette, T., Hervig, R. L. & Holloway, J. R. Trace element partitioning between amphibole, phlogopite, and basanite melt. *Earth Planet. Sci. Lett.* **135**, 13–30 (1995).
26. Davidson, J., Turner, S. & Plank, T. Dy/Dy*: Variations arising from mantle sources and petrogenetic processes. *J. Petrol.* **54**, 525–537 (2013).
27. Yoder, H. & Tilley, C. Origin of basalt magmas: an experimental study of natural and synthetic rocks systems. *J. Petrol.* **3**, 342–532 (1962).
28. O'Hara, M. J. & Yoder, H. S. Formation and fractionation of basic magmas at high pressures. *Scott. J. Geol.* **3**, 67–117 (1967).
29. Clague, D. A. Hawaiian alkaline volcanism. *Geol. Soc. Lond., Spec. Publ.* **30**, 227–252 (1987).
30. Mallik, A. & Dasgupta, R. Reactive infiltration of MORB-eclogite-derived carbonated silicate melt into fertile peridotite at 3 GPa and genesis of alkalic magmas. *J. Petrol.* **54**, 2267–2300 (2013).
31. White, A. J. R., Chappel, B. W. & Jakes, P. Coexisting clinopyroxene, garnet and amphibole from an “eclogite”, Kakanui, New Zealand. *Contributions Mineral. Petrol.* **34**, 185–191 (1972).
32. Devey, C. W., Lackschewitz, K. S., Mertz, D. F., Bourdon, B., Cheminee, J. L., Dubois, J., Guivel, C., Hekinian, R. & Stoffers, P. Giving birth to hotspot volcanoes: Distribution and composition of young seamounts from the seafloor near Tahiti and Pitcairn islands. *Geol. Soc. Am.* **31**, 395–398 (2003).
33. Klügel, A. & Klein, F. Complex magma storage and ascent at embryonic submarine volcanoes from the Madiera Archipelago. *Geology* **34**, 337–340 (2006).
34. Klügel, A., Longpre, M. A., Garcia-Canada, L. & Stix, J. Deep intrusions, lateral magma transport and related uplift at ocean island volcanoes. *Earth Planet. Sci. Lett.* **431**, 140–149 (2015).
35. Gleeson, M. L., Gibson, S. A. & Stock, M. J. Upper mantle mush zones beneath low melt flux ocean island volcanoes: insights from Isla Floreana, Galápagos. *J. Petrol.* **61**, ega094 (2020).
36. Dasgupta, R., Hirschmann, M. M. & Smith, N. D. Partial melting experiments of peridotite + CO₂ at 3 GPa and genesis of alkalic ocean island basalts. *J. Petrol.* **48**, 2093–2124 (2007).
37. Li, X., Kind, R., Priestley, K., Sobolev, S. V., Tilmann, F., Yuan, X. & Weber, M. Mapping the Hawaiian plume conduit with converted seismic waves. *Nature* **405**, 938–941 (2000).
38. Anderson, D. L. Hawaii, boundary layers and ambient mantle-geophysical constraints. *J. Petrol.* **52**, 1547–1577 (2011).
39. Tilling, R. I. & Dvorak, J. J. Anatomy of a basaltic volcano. *Nature* **363**, 125–133 (1993).
40. Wright, T. L. & Klein, F. W. Deep magma transport at Kilauea volcano, Hawaii. *Lithos* **87**, 50–79 (2006).
41. Wech, A. G. & Thelen, W. A. Linking magma transport structures at Kilauea volcano. *Geophys. Res. Lett.* **42**, 7090–7097 (2015).
42. Bizimis, M., Sen, G., Salters, V. J. M. & Keshav, S. Hf-Nd-Sr isotope systematics of garnet pyroxenites from Salt Lake Crater, Oahu, Hawaii: Evidence for a depleted component in Hawaiian volcanism. *Geochim. Cosmochim. Acta* **69**, 2629–2646 (2005).
43. King, S. A. & Adam, C. Hotspot swells revisited. *Phys. Earth Planet. Inter.* **235**, 66–83 (2014).
44. Coombs, M. L., Sisson, T. W. & Lipman, P. W. *Major-element, sulfur, and chlorine compositions of glasses from the submarine flank of Kilauea volcano, Hawaii, collected during 1998–2002 Japan Marine Science and Technology Centre (JAMSTEC) Cruises*. United States Geological Survey Open Report 1378 (2004).
45. O'Neill H.St.C. The thermodynamic controls on sulfide saturation in silicate melts with application to ocean floor basalts. In *Magma Redox Geochemistry* (eds Moretti, R. & Neuville, D. R.) 266, 177–213 (American Geophysical Union, 2021).
46. Sinton, J. M., Ford, L. L., Chappel, B. & McCulloch, M. T. Magma genesis and mantle heterogeneity in the Manus back-arc basin, Papua New Guinea. *J. Petrol.* **44**, 159–195 (2003).
47. Le Losq, C., Neuville, D. R., Moretti, R. & Roux, J. Determination of water content in silicate glasses using Raman spectrometry, with application to explosive volcanism. *Am. Mineralogist* **97**, 779–790 (2012).
48. Lowenstern, J. B. & Pitcher, B. W. Analysis of H₂O in silicate glass using attenuated total reflectance (ATR) micro-FTIR spectroscopy. *Am. Mineralogist* **98**, 1660–1668 (2013).
49. Mare, E. R., O'Neill, H. St. C., Berry, A. J., Frigo, C. & Glover, C. J. Coordination change of Ge⁴⁺ and Ga³⁺ in silicate melt with pressure. *Geochim. Cosmochim. Acta* **303**, 184–204 (2021).
50. Jenner, F. E. & O'Neill, H. St. C. Major and trace analysis of basaltic glasses by laser-ablation ICP-MS. *Geochem., Geophys., Geosyst.* **13**, GC003890 (2012).
51. Branson, O., Fehrenbacher, J. S., Vetter, L., Sadekov, A. Y., Eggins, S. M. & Spero, H. J. LAtools: A data analysis package for the reproducible reduction of LA-ICPMS data. *Chem. Geol.* **504**, 83–95 (2019).

Acknowledgements

We thank Tom Sisson for providing the samples, Peter Reiners for providing a copy of his reactive flow spreadsheet, and the Australian Research Council for the award of grant FL130100066 to H.O.N.

Author contributions

L.M. performed the modelling, carried out the experimental and analytical work, and wrote the manuscript; H.O.N. and A.B. both contributed significantly to the modelling and manuscript; C.L. recorded and interpreted the ATR-FTIR spectra.

Competing interests

The authors declare no competing interests.

Additional information

Supplementary information The online version contains supplementary material available at <https://doi.org/10.1038/s41467-022-30108-x>.

Correspondence and requests for materials should be addressed to Laura A. Miller.

Peer review information *Nature Communications* thanks Jon Blundy and the anonymous reviewer(s) for their contribution to the peer review of this work.

Reprints and permission information is available at <http://www.nature.com/reprints>

Publisher's note Springer Nature remains neutral with regard to jurisdictional claims in published maps and institutional affiliations.



Open Access This article is licensed under a Creative Commons Attribution 4.0 International License, which permits use, sharing, adaptation, distribution and reproduction in any medium or format, as long as you give appropriate credit to the original author(s) and the source, provide a link to the Creative Commons license, and indicate if changes were made. The images or other third party material in this article are included in the article's Creative Commons license, unless indicated otherwise in a credit line to the material. If material is not included in the article's Creative Commons license and your intended use is not permitted by statutory regulation or exceeds the permitted use, you will need to obtain permission directly from the copyright holder. To view a copy of this license, visit <http://creativecommons.org/licenses/by/4.0/>.

© The Author(s), corrected publication 2022